Graphene quantum dot enabled interlayer spacing and electronic structure regulation of single-atom doped MoS_2 for efficient alkaline hydrogen evolution

Jun Gong[a‡], Zheye Zhang[a‡], Shibo Xi[b], Wenjun Wang[c], Jianmei Lu[d], Peng Chen[a,*]

[a]School of Chemical & Biomedical Engineering, Nanyang Technological University, 70 Nanyang Drive, 637457, Singapore

[b]Institute of Sustainability for Chemicals, Energy and Environment, Agency for Science, Technology and Research (A*STAR), 1 Pesek Road, Singapore 627833, Singapore

[c]School of Physical Science and Information Technology, Liaocheng University, Liaocheng 252059, China

[d]College of Chemistry, Chemical Engineering and Materials Science, Collaborative Innovation Center of Suzhou Nano Science and Technology, Soochow University, Suzhou 215123, China

[‡]These authors contributed equally to this work.

*Corresponding Author: Peng Chen; E-mail: chenpeng@ntu.edu.sg

KEYWORDS: Interlayer engineering, Graphene quantum dots, Molybdenum disulfide, Single-atom catalysts, Hydrogen evolution reaction

ABSTRACT: Interlayer engineering of two-dimensional (2D) materials is believed to be a key to enhance their performance for catalysis and other applications. Herein, molybdenum disulfide intercalated with heteroatom-doped graphene quantum dots and individually dispersed Co atoms (GQD/Co-MoS_2) is readily synthesized by a one-pot hydrothermal reaction. With better long-

term stability, GQD/Co-MoS_2 shows comparable catalytic performance as commercial Pt/C catalyst for hydrogen evolution reaction in alkaline medium at low current densities (overpotential of 53 *vs.* 44 mV at 10 mA cm^{-2}) and outperforms Pt/C at high current densities (106 *vs.* 172 mV at 100 mA cm^{-2}). Based on both experimental and theoretical investigations, the outstanding performance is mainly attributed to the enlarged interlayer spacing and electronic coupling at the 0D/2D van der Waals heterojunctions between GQDs and Co-doped MoS_2. In principle, a variety of GQD intercalated 2D materials with atomic doping of one or more metallic elements can be similarly synthesized for diverse applications.

1. Introduction

Hydrogen production by electrochemical water splitting is a carbon-free process to produce high-energy density fuel alternative to fossil fuels [1-3]. Towards low-cost scale-up production, tremendous effort has been paid to search for non-precious electrocatalysts for hydrogen evolution reaction (HER), including earth-abundant two-dimensional material molybdenum disulfide (MoS_2) [4-6]. The catalytic performance of MoS_2 is, however, compromised by its poor electron conductivity and limited edge-active sites on the inert basal plane [7]. Introducing conductive carbon nanomaterials into MoS_2-based catalysts could promote electron transfer and boost the HER performance [8,9]. Single-layered MoS_2 sheets outperform their bulk counterparts, but their synthesis is non-trivial and costly. Moreover, most MoS_2-based catalysts work in acidic electrolytes because in basic media an additional reaction step is required to break the strong H-O-H bonds prior to the adsorption of H* [10]. However, in acidic media, the water splitting process suffers from vessel corrosion, the sluggish kinetics of oxygen evolution reaction (OER) at the counter electrode, poor stability, and the need of expensive proton-exchange

membrane [11]. Thus, devising low-cost MoS_2 electrocatalysts with enhanced HER performance in alkaline environment is highly desirable. Increasing the interlayer spacing has been reported as an effective way to improve the catalytic performance of MoS_2 by facilitating electron and proton transfer [12,13]. Oxygen, hydrogen and ammonium have been used as the molecular intercalation agents to increase the interlayer spacing of MoS_2 through in situ incorporation during hydrothermal process [14-17]. However, these methods are limited by instability of the intercalation, safety concern, and poor controllability.

Graphene quantum dots (GQDs) are a family of atomically-thin graphitic structures with lateral dimensions typically <10 nm, exhibiting unique potentials in catalysis, imaging, sensing, energy conversion and storage [18,19]. We have previously demonstrated the use of GQDs as the intercalation agent to exfoliate single-layered 2D materials from their bulk forms simply by mild sonication, utilizing their atomic thickness and intimate interaction with 2D materials [20,21]. Furthermore, the as-formed GQD/2D material hybrids with 0D/2D van der Waals heterojunctions (vdWHs) exhibit enhanced catalytic properties. Single-atom catalysts (SACs) have attracted much interest because of full utilization of the catalytic sites and highly tunable properties by tailoring the coordination environment [22-24]. Doping single metal atoms onto the inert basal plane of MoS_2 can largely improve its HER activity [25,26]. The strong bonding with sulphur atoms prevents the metal atoms from forming clusters or particles. The synthesis of SAC-MoS_2 catalysts is, however, tedious and of low yield.

In this contribution, we for the first time demonstrate a simple one-pot hydrothermal synthesis of GQD intercalated MoS_2 with doping of single Co atoms (GQD/Co-MoS_2). For HER, the GQD/Co-MoS_2 catalyst with a much enlarged interlayer spacing of 9.7 Å gives a current density of 10 mA cm^{-2} at an overpotential as low as 53 mV, greatly outperforming the GQD-free

counterparts (138 mV). Based on comprehensive experimental and theoretical evidence, the superior HER catalytic activities are attributed to abundantly exposed active sites and unhindered transport of reactants because of greatly increased interlayer spacing, promoted charge transfer at GQD/MoS_2 0D/2D vdWHs, and reduced electronic bandgap. In principle, this strategy may be adopted to synthesize a variety of GQD-intercalated and single-metal-atom-doped catalysts with 0D/2D vdWHs for various catalysis and energy applications.

2. Experimental methods

2.1. Materials

Ammonium molybdate tetrahydrate ($(NH_4)_6Mo_7O_{24}\cdot 4H_2O$), cobaltous nitrate hexahydrate ($Co(NO_3)_2\cdot 6H_2O$), thiourea (CH_4N_2S), potassium hydroxide (pellets, 99.99% trace metals basis), Nafion solution (5 %), nickel (II) nitrate hexahydrate ($Ni(NO_{3)2}\cdot 6H_2O$), Pt/C (20 wt.%), carbon black, absolute ethanol (100%) and citric acid ($C_6H_8O_7$) were purchased from Sigma Aldrich (Singapore) and utilized without further purification.

2.2. Sample preparation

A modified method was used to prepare GQD based on the previous reports [27,28]. Specifically, a mixture of $C_6H_8O_7$ (6.5 mmol) and CH_4N_2S (8 mmol) was dispersed in 20 mL deionized water (diH_2O) and then sealed into a Teflon autoclave for 20 h hydrothermal treatment at 175 ˚C. Next, the resulting solution was centrifuged at 12000 rpm for 30 min to obtain the supernatant. After dialysis (MWCO 500 Da) for 2 days, the solution was purified by 0.22 μm syringe filter to remove aggregates. Finally, GQD powder was obtained after freeze-drying the solution. To synthesize MoS_2 based hybrid catalysts, a mixture of $C_6H_8O_7$ (6.5*n* mmol), CH_4N_2S (7.5 + 8*n* mmol), $(NH_4)_6Mo_7O_{24}\cdot 4H_2O$ (0.25 mmol), $Co(NO_3)_2\cdot 6H_2O$ (0.2 mmol) was dissolved in 20 mL diH_2O with vigorous stirring, which was then transferred into a Teflon autoclave for

20h hydrothermal treatment at 175 ˚C. For the synthesis of Co-MoS_2, GQD/Co-MoS_2-l, GQD/Co-MoS_2, GQD/Co-MoS_2-h, n=0, 0.5, 1 and 2, respectively. The product was then centrifuged at 4000 rpm for 30 min. The obtained sediment was subsequently washed by ethanol/diH_2O and then fully withered at 60 ˚C under vacuum. To synthesize MoS_2, GQD/MoS_2-l, GQD/MoS_2, GQD/MoS_2-h, the same procedure was applied without adding $Co(NO_3)_2 \cdot 6H_2O$. Ni-MoS_2, GQD/Ni-MoS_2-l, GQD/Ni-MoS_2, GQD/Co-MoS_2-h were similarly synthesized by replacing $Co(NO_3)_2 \cdot 6H_2O$ with $Ni(NO_3)_2 \cdot 6H_2O$ (0.2 mmol).

2.3. Characterizations

Field-emission electron microscope (FESEM, JEOL JSM-6700), atomic force microscopy (AFM, Bruker ICON), and high-resolution transmission electron microscope (HRTEM, JEM 2100PLUS) were used to reveal the morphology of synthesized materials. High-resolution high-angle annular dark field (HADDF) scanning transmission electron microscopy (STEM) was performed using Tian Cube Themis G2300 with STEM aberration (Cs) corrector operated at 200 kV. The crystal structures were characterized by wide-angle X-ray diffraction (XRD, Bruker D2 Advance) with Cu Kα radiation (λ = 1.5406 Å). The elemental composition was investigated by X-Ray photoelectron spectroscope (XPS, Shimadzu Kratos Axis Supra) equipped with a monochromatic Al/Ag Kα X-ray source, with all binding energies being gauged to C 1s peak centered at 284.8 eV. An INCA X-ray microanalysis system equipped on the JEOL 2100F microscope was adopted for energy-dispersive X-ray (EDX) analysis. Raman spectra were obtained by a Renishaw InVia Reflex with 633 nm excitation. Fourier-transform infrared (FTIR) spectroscopy was conducted by a PerkinElmer FTIR spectrometer (Spectrum One). X-ray absorption near edge structure (XANES) spectra and X-ray absorption near edge structure (XANES) spectra at Co K-edge were obtained using the XAFCA beamline of the Singapore

Synchrotron Light Source in transmission mode. Co_3O_4 and Co foil were used as the references. Athena and Artemis contained in the Demeter package were used for data analysis.

2.4. Electrochemical measurements

All electrochemical tests were conducted with an electrochemical workstation (CHI 760D, CH Instruments). Catalysis of hydrogen evolution reaction (HER) was performed in Ar (99.99%)-saturated 1 M KOH solution, using a glassy carbon rotating disk electrode (RDE) with diameter of 5 mm as the working electrode, a graphite rod as the counter electrode, and an Ag/AgCl electrode in saturated KCl solution as the reference electrode. All potentials were referenced to reversible hydrogen electrode (RHE) following the equation $E_{RHE} = E_{Ag/AgCl} + 0.059pH + 0.197$. For all i–E curves, the solution resistance R was determined from auto iR compensation by setting the test potential, step amplitude, compensation level as 0 V, 0.05V, 100%, respectively. To prepare the electrocatalyst inks, 4 mg carbon black and 8 mg catalyst were added into a mixture of 60 μL Nafion and 940 μL 1:1 water-ethanol solution, followed by 2h ultrasonication. Then 10 μL catalyst ink was drop-casted on the surface of a freshly polished RDE and the loading mass is 0.4 mg cm^{-2}. With a rotation speed of 1600 rpm, linear sweep voltammograms (LSVs) were obtained under a scan rate of 5 mV s^{-1} with iR drop correction. Double layer capacitance (C_{dl}) was calculated based on the obtained cyclic voltammograms under different scan rates (20-120 mV s^{-1}). Electrochemical impedance spectroscopy (EIS) was obtained at a bias of -0.235 V vs. RHE in a frequency range of 1-100 kHz with an amplitude of 5 mV.

2.5. Theoretical calculations

Vienna Ab initio Simulation Package (VASP) was applied to conduct first principle density functional theory (DFT) calculations and the generalized gradient approximation was expressed

using the Perdew-Burke-Ernzerhof (PBE) functional. A kinetic energy cut-off for the plane wave basis was set as 450 eV to optimize the ionic cores and valence electrons under the projected augmented wave (PAW) potentials. The force convergency for geometry optimizations was set below 0.05 $eVÅ^{-1}$. All surface calculations were performed using 2×2×1 Monkhorst-Pack k-points sampling and all the adsorption energies were alluded to the energies of gas phase H_2O and H_2. All the calculated energies were corrected based on the free energy at 300 K. The chemical potential of OH^- was calculated using the following equation under U = 0 V vs RHE: $G(OH^-) = G(H_2O) – 1/2G(H_2)$.

3. Results and discussions

3.1. Synthesis and characterizations of catalysts

Both GQD and MoS_2 can be synthesized based on fusion of small precursor molecules under hydrothermal conditions [27-29]. Such bottom-up synthesis gives good product homogeneity and ease to dope heteroatoms. Using citric acid as the precursor and thiourea as the source of N and S dopants, single- or double layered N,S-doped GQDs (~6.1 nm in diameter) can be hydrothermally produced at 175 ˚C for 20 h (Fig. S1, S2). Using ammonium molybdate tetrahydrate and thiourea as the precursor and cobaltous nitrate hexahydrate as the source of Co dopant, Co-doped MoS_2 nanoflowers (Co-MoS_2, ~500 nm) were produced under the same hydrothermal condition (Fig. S3, S4). As illustrated in Fig. 1a, N,S-doped GQDs and Co-MoS_2 can be synthesized simultaneously in presence of all the precursors. Thiourea serves as the S source for both MoS_2 formation and GQD doping. Conceivably, because of vdW interaction and sharing of S atom between N,S-doped GQD and MoS_2 layer, GQDs shall intercalate between MoS_2 layers to form GQD/Co-MoS_2 nanoflowers. The amount of GQDs in the hybrid can be

adjusted by halving (GQD/Co-MoS_2-l) or doubling (GQD/Co-MoS_2-h) its precursor concentrations.

As shown in Fig. 1b, X-ray diffraction (XRD) pattern of commercial bulk MoS_2 has two peaks at 14.4˚ and 32.7˚ attributed by the (002) and (100) planes of MoS_2 (JCPDS card no. 37–1492). In comparison, XRD pattern of synthesized Co-MoS_2 exhibits broadened peaks because of decreased crystallinity and a small left-shifted (002) peak presumably due to Co doping [30]. The (002) peaks of GQD/Co-MoS_2-l, GQD/Co-MoS_2, GQD/Co-MoS_2-h left-shifted greatly, indicating that the interlayer spacing is significantly enlarged by GQDs in a dose-dependent manner and saturates at 9.7 Å (Fig. 1b and Table S1) [14-17]. The characteristic XRD peak from Co crystal is absent, implying that Co atoms are individually dispersed. The XRD peak from carbon is also missing due to the low abundance of GQDs. As illustrated in Fig. 1c, the vdW gap [31] between adjacent MoS_2 layers increases from 2.1 to 5.3 Å, which is larger than a water molecule (~4 Å). As previously reported [12,13,16], expanded interlayer spacing of MoS_2 allows exposure of non-edge catalytic sites and interlayer mass (water) transport during HER catalysis.

As seen from the scanning electron microscope (SEM) and transmission electron microscope (TEM) images in Fig. 2a and Fig. S5, GQD/Co-MoS_2 shows similar flowerlike morphology assembled by thin sheets as that of Co-MoS_2, suggesting that introduction of GQDs does not cause any noticeable morphology alteration. High-resolution TEM (HRTEM) image reveals a large interlayer spacing of 9.7 Å for MoS_2 and a lattice distance of 3.5 Å which can be assigned to the (002) facet of GQDs (Fig. 2b). The diameter of the GQDs attached on MoS_2 sheet is similar to that of the GQDs synthesized alone (Fig. S1b). Before TEM imaging, the samples have to be sonicated. Therefore, it is not surprising that some of the sandwiched structures (MoS_2 with GQD intercalation) are disrupted, so that, TEM is able to identify the exposed GQDs. As shown

in Fig. S6, GQD/Co-MoS_2-l and GQD/Co-MoS_2-h with similar flowerlike morphology exhibit enlarged interlayer spacings of 8.7 Å and 9.7 Å, respectively. In addition, similar interlayer expanding can also be observed in GQD/MoS_2-l, GQD/MoS_2 and GQD/MoS_2-h without Co doping (Fig. S7). The interlayer spacings measured by HRTEM match well with the XRD analyses, confirming the significant expansion of interlayer spacing due to GQD intercalation. Note that no nanoparticles or clusters are visible from the HRTEM images, indicating that Co atoms are individually dispersed. High-angle annular dark-field scanning TEM (HAADF-STEM) with atomic resolution (Fig. 2c,d) and the corresponding intensity line profiles (Fig. 2e) further demonstrate that Co atoms are individually doped into the MoS_2 lattice, and both 1T and 2H phases of MoS_2 co-exist [32,33]. Energy-dispersive X-ray (EDX) elemental mapping demonstrates the homogeneous distributions of Mo, S, C, N, and Co elements in GQD/Co-MoS_2 (Fig. 2f).

The Raman spectrum of commercial bulk MoS_2 shows two prominent 2H-phase peaks centered at 375 (E^1_{2g}) and 403 (A_{1g}) cm^{-1} (Fig. 3a), arising from the in-plane and out-plane Mo-S vibration at edge sites, respectively [34]. For synthesized samples, in addition to the 2H-phase peaks at 283 (E_{1g}) and 375 (E^1_{2g}) cm^{-1}, 1T-phase peaks at 146 (J_1), 236 (J_2) and 335 (J_3) cm^{-1} emerge [35]. Mo-S vibration signal (A_{1g}) of 2H-MoS_2 is missing, suggesting that the edge sites of all synthesized samples are 1T phase instead of 2H phase. This is desirable because edge sites are more catalytically active than basal plane and metallic 1T-MoS_2 exhibit much better HER performance than semiconducting 2H-MoS_2 [8,36,37].

The X-ray photoelectron spectroscopy (XPS) spectrum of commercial bulk MoS_2 exhibits two characteristic peaks located at 233.0 and 229.9 eV, corresponding to Mo $3d_{3/2}$ and Mo $3d_{5/2}$ of 2H-phase MoS_2, respectively (Fig. 3b) [38]. The synthesized samples present two additional

peaks ascribable to the formation of 1T phase, agreeing with the Raman analysis. Mo 3d of Co-MoS_2 shows a positive shift of 0.2 eV compared to MoS_2, while an even larger shift (0.35 eV) is observed with introduction of GQD in GQD/Co-MoS_2-l. With an increased amount of GQDs, GQD/Co-MoS_2 shows additional 0.15 eV positive shift compared to GQD/Co-MoS_2-l. But such shift saturates when the amount of GQDs increases further as observed from GQD/Co-MoS_2-h. The progressive positive shift of Mo 3d binding energy with introduction of Co and GQD into the hybrids suggests charge transfer from MoS_2 to both Co and GQD, and such electronic coupling is stronger with increasing amount of GQDs. The existence of Co is further demonstrated by the Co 2p spectrum (Fig. 3c), which is deconvoluted into two peaks of Co $2p_{3/2}$ and Co $2p_{1/2}$ at 782.3 eV and 797.6 eV, respectively. The peaks located at 779.4 eV and 794.3 eV are assigned to Co-S bond [25].

To investigate the local coordination environment of Co atoms, X-ray absorption spectroscopy (XAS) was conducted. X-ray absorption near edge structure (XANES) spectra at Co K-edge (Fig. 3d) reveal that the absorption edge of GQD/Co-MoS_2 is located between those from Co foil and CoO, suggesting that the valence state of Co may be between 0 and +2. The Fourier transform k^2-weighted extended X-ray absorption fine structure (EXAFS) spectrum of GQD/Co-MoS_2 (Fig. 3e) shows only one prominent peak at 1.76 Å, corresponding to Co-S first coordination shell formed due to doping of Co into MoS_2 lattice [39]. No Co-Co peak (2.15 Å) or other high-shell peaks are observed, further confirming the single-atomic nature of Co existence. Quantitative EXAFS fitting suggests that a Co atom in GQD/Co-MoS_2 is coordinated by four S atoms (Fig. 3f and Table S2).

3.2. Electrocatalytic HER performance

The HER performance was evaluated using rotating disk electrodes in Ar-saturated 1 M KOH electrolyte. As shown in Fig. 4a, the overpotential of Co-MoS_2 (138 mV) at 10 mA cm^{-2} is much smaller compared to that of MoS_2 (322 mV), indicating the beneficial roles of Co doping. Actually, it has been shown that Co-SACs are catalytically active for HER [24,25]. With expanded interlayer spacing due to GQD intercalation, the overpotential of GQD/Co-MoS_2 further reduced to 53 mV, comparable to that of Pt/C (44 mV). It is noteworthy that GQD/Co-MoS_2 outperforms Pt/C at high current densities (e.g., 106 vs. 172 mV at 100 mA cm^{-2}), suggesting its high potential for practical application. Comparing to GQD/Co-MoS_2, excess introduction of GQDs in GQD/Co-MoS_2-h does not further increase the interlayer spacing, instead it undesirably causes increase of overpotential to 81 mV conceivably due to over-coverage on the active sites. The enhancement of HER performance by Co-doping and its correlation with interlayer spacing are summarized in Fig. 4b and further corroborated by the HER experiments using GQD/MoS_2 catalysts without Co-doping (Fig. S8, S9). From XPS results, the doping amount of Co in GQD/Co-MoS_2 is as high as 3.93 wt%. Further increase of Co content would likely compromise HER activity due to formation of Co nanoparticles [40]. In addition to enlarging the interlayer spacing, N,S-doped GQDs themselves may have intrinsic HER activity [20]. As depicted in Fig. 4c, introduction of single atom Co in MoS_2 has negligible impact on the Tafel slope. In contrast, with introduction of GQDs in Co-MoS_2, the Tafel slope of GQD/Co-MoS_2 significantly decreases to 53.8 mV dec^{-1}, suggesting a faster HER kinetics which follows the Volmer-Heyrovsky mechanism [41]. GQD/Co-MoS_2 outperforms the state-of-the-art Co- or MoS_2- based non-precious metal electrocatalysts (Fig. 4d and Table S3).

Nyquist plots from electrochemical impedance spectroscopy (EIS) in Fig. 4e reveal that GQD/Co-MoS_2 exhibits the smallest charge-transfer resistance (R_{ct}) in all samples, implying that

its superior performance is partly attributable to the fast charge transfer at catalyst surface. The XPS results show that GQD/Co-MoS_2 has a large binding energy shift of Mo 3d owing to strong electronic coupling between Co-MoS_2 and attached GQDs. Such intimate coupling at the 0D/2D van der Waals heterojunctions (vdWHs) promotes charge transfer because of reduced Schottky barrier [20,21]. Electrochemically active surface area (ECSA) is reflected by double layer capacitance (C_{dl}). GQD/Co-MoS_2 displays the largest double layer capacitance (C_{dl}) of 5.89 mF cm^{-2}, suggesting the highest ECSA among all the catalysts (Fig. 4f, Fig. S10). C_{dl} of GQD/Co-MoS_2-h is smaller (3.82 mF cm^{-2}), implying that its inferior catalytic performance is attributable to reduced ECSA because of excess coverage by GQDs. Even though GQDs may have certain intrinsic HER activity, the benefit brought by more GQDs could not compensate the compromise caused by too much coverage of active sites on MoS_2. Apart from the superior electrocatalytic activity, GQD/Co-MoS_2 exhibits excellent long-term durability as compared with the commercial Pt/C catalyst (Fig. 4g). The post-HER characterizations showed that the structure and composition of GQD/Co-MoS_2 were well-preserved after the durability test (Fig. S11).

GQD intercalated MoS_2 with doping of Ni single atoms have also been synthesized simply by replacing $Co(NO_3)_2 \cdot 6H_2O$ with $Ni(NO_3)_2 \cdot 6H_2O$ as the source of Ni dopants (Fig. S12, Fig. S13a). As shown in Fig. S13b-S15, with the optimal GQD loading, GQD/Ni-MoS_2 outperforms GQD/MoS_2 but is inferior to GQD/Co-MoS_2 (114 vs. 53 mV at 10 mA cm^{-2}). However, GQD/Ni-MoS_2 may be advantageous for other catalytic reactions. Our method can be used to synthesize a variety of GQD/2D Material catalysts with atomic doping of one or more metallic species.

3.3. DFT theoretical investigation

Density functional theory (DFT) calculations were performed to unveil the catalytic mechanisms. It was found that edge S atoms of MoS_2 are the most stable adsorption sites for H* intermediate, consistent with the previously reported Co-doped MoS_2 catalysts [16,42]. The reaction steps and the interactions between GQD/Co-MoS_2 and reaction intermediates (H* and OH*) are illustrated in Fig. 5a. In an alkaline solution, dissociating the water molecules adsorbed on the catalyst is the first and crucial step. As shown in Fig. 5b, it is the rate-limiting step and the associated energy barrier is reduced from 1.122 eV on MoS_2 to 0.439 eV on Co-MoS_2 and further to 0.125 eV on GQD/Co-MoS_2, which explains their performance difference as observed experimentally. Electron density difference maps (Fig. 5c,d) reveal the charge transfer from Mo to Co and GQD. This significantly increases acticoncentration at MoS_2 surface or GQD-MoS_2 interface, whereby enhancing the catalytic activity. The calculated density of states (DOS) in Fig. 5e shows that Co-MoS_2 and GQD/Co-MoS_2 exhibit zero bandgap. Such semimetal characteristics are resulted from the high content of 1T-MoS_2 phase. Notably, DOS of GQD/Co-MoS_2 demonstrates a higher density state at Fermi level as compared to that of Co-MoS_2, suggesting a stronger electron mobility and hence more efficient charge transfer. This is consistent with the XPS and EIS results which show that there is strong charge transfer from MoS_2 to Co and GQD in GQD/Co-MoS_2. In addition, the projected density of states (PDOS) in Fig. 5f reveal that the higher density state at Fermi level of GQD/Co-MoS_2 is mainly caused by the complete band structure transition of Co from semiconducting to metallic phase due to the introduction of GQDs. Taken together, the theoretical calculations suggest that the superior catalytic performance of GQD/Co-MoS_2 is attributable to the higher conductivity and faster charge transfer kinetics.

4. Conclusion

In summary, we have demonstrated a facile strategy for interlayer engineering of 2D materials. Specifically, GQD intercalated MoS_2 catalyst with controllably enlarged interlayer spacing and doped Co single atoms in the lattice (GQD/Co-MoS_2) is produced by a one-pot hydrothermal synthesis. For hydrogen evolution reaction (HER), GQD/Co-MoS_2 catalyst shows comparable catalytic performance as Pt/C at low current density (overpotential of 53 *vs.* 44 mV at 10 mA cm^{-2}) and outperforms it at high current density (106 *vs.* 172 mV at 100 mA cm^{-2}). The outstanding performance is attributable to the enlarged interlayer spacing (9.7 Å) that allows full exposure of active sites and unblocked mass transport. In addition, the catalytic activity is also benefitted from the high conductivity due to high content of 1T-phase MoS_2, electron enrichment at MoS_2 due to charge transfer to Co and GQD, fast charge transfer at GQD/MoS_2 vdW heterojunctions because of reduced Schottky barrier, and the intrinsic catalytic property of heteroatom-doped GQDs and Co single atoms. GQDs are a family of nanocarbon materials covering a wide range of properties. In principle, a variety of GQD intercalated 2D materials with atomic doping of one or more metallic elements can be similarly synthesized for different catalysis and energy applications.

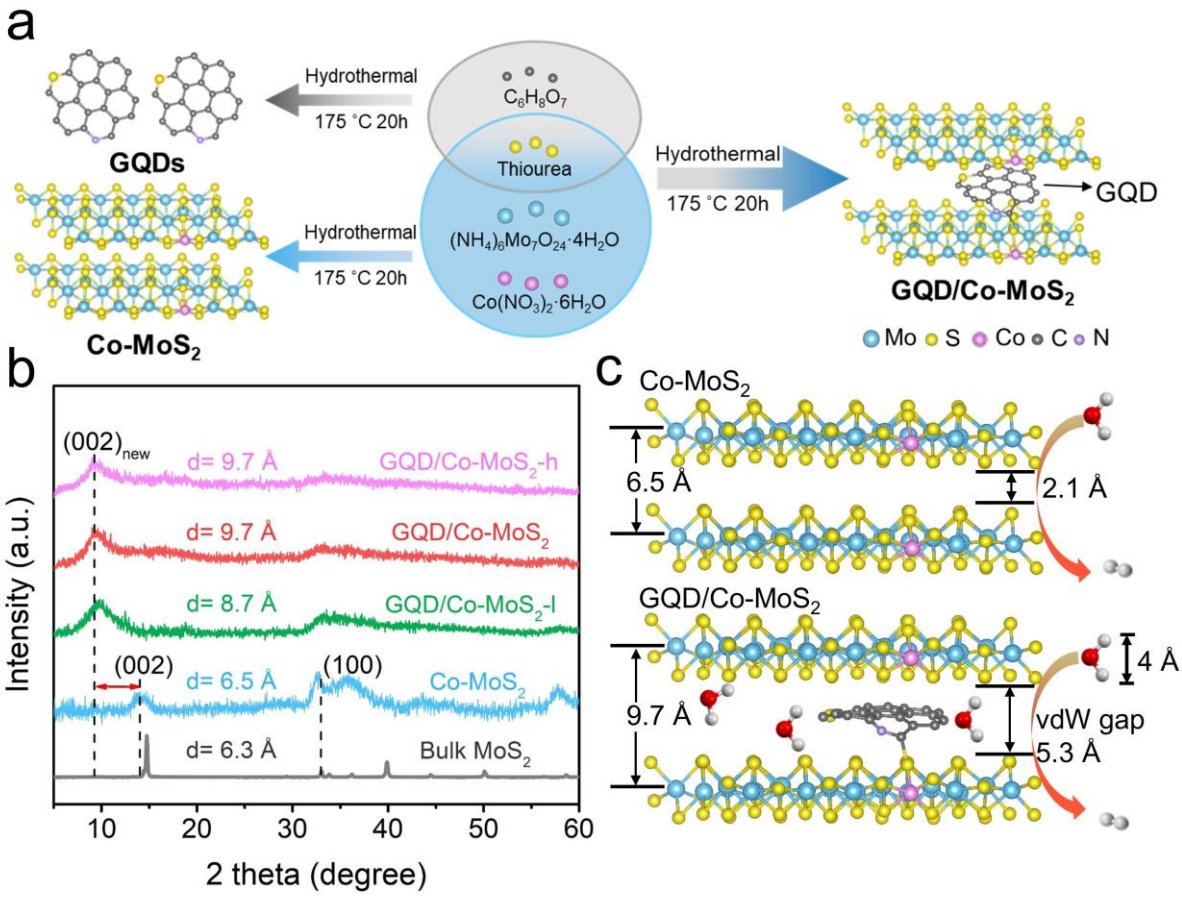

Fig. 1. Synthesis of GQD intercalated MoS_2 with Co-doping. (a) Schematic illustration of the synthesis of GQDs, Co-MoS_2 and GQD/Co-MoS_2; (b) XRD patterns of commercial bulk MoS_2, and synthesized Co-MoS_2, GQD/Co-MoS_2-l, GQD/Co-MoS_2, GQD/Co-MoS_2-h. l and h refer to the use of low and high concentrations of GQD precursors, respectively; (c) Side-view of the crystal structures of Co-MoS_2 and GQD/Co-MoS_2.

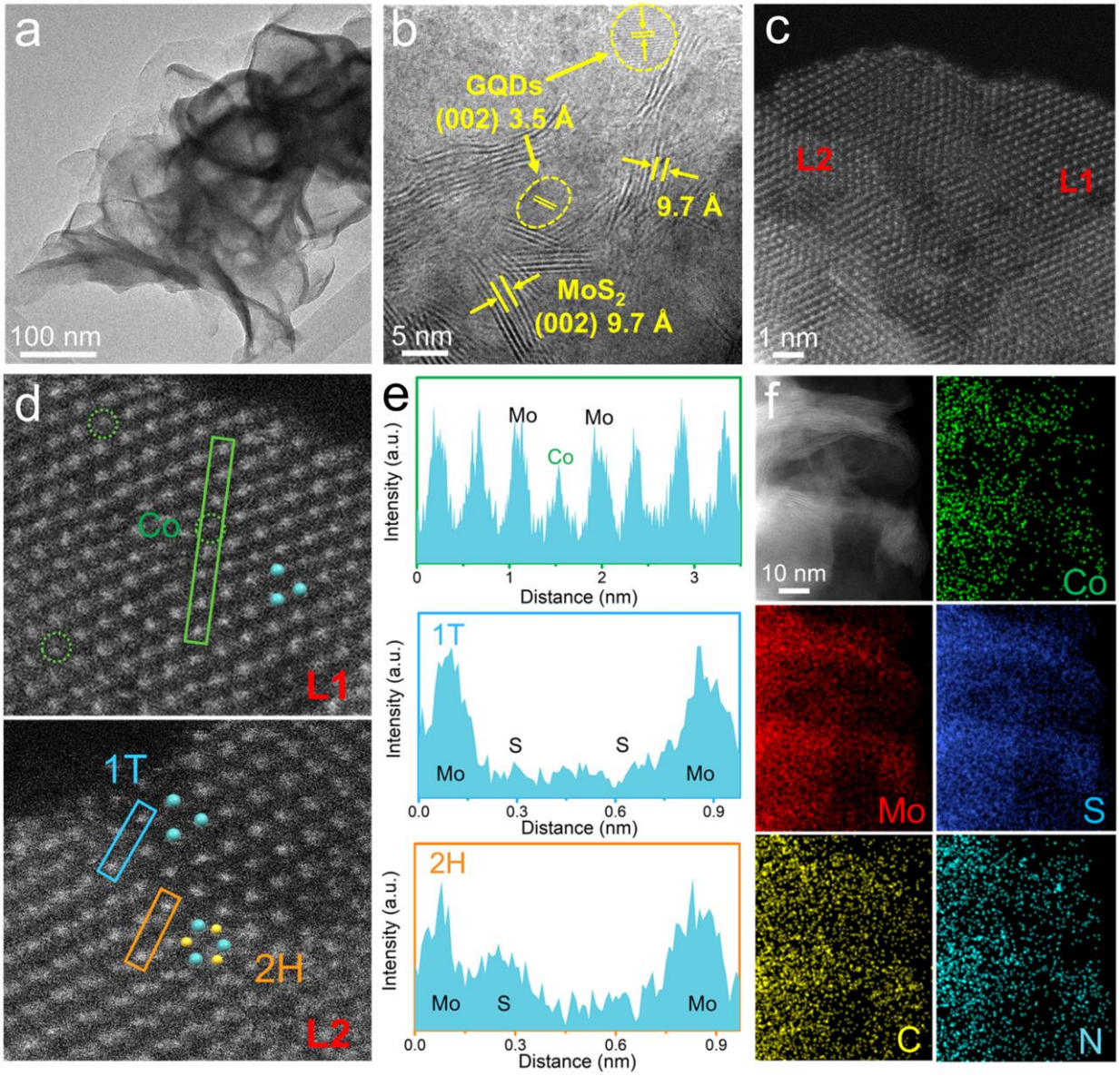

Fig. 2. Electron microscopy of GQD/Co-MoS_2. (a) TEM, (b) HRTEM and (c) HAADF-STEM images; (d) Magnified L1 and L2 domains in (c), demonstrating individual Co atoms, 1T and 2H phases of MoS_2; Green, blue and yellow balls indicate Co, Mo and S atoms, respectively; (e) Corresponding linear intensity profiles of the indicated lines in (d); (f) EDX element mapping.

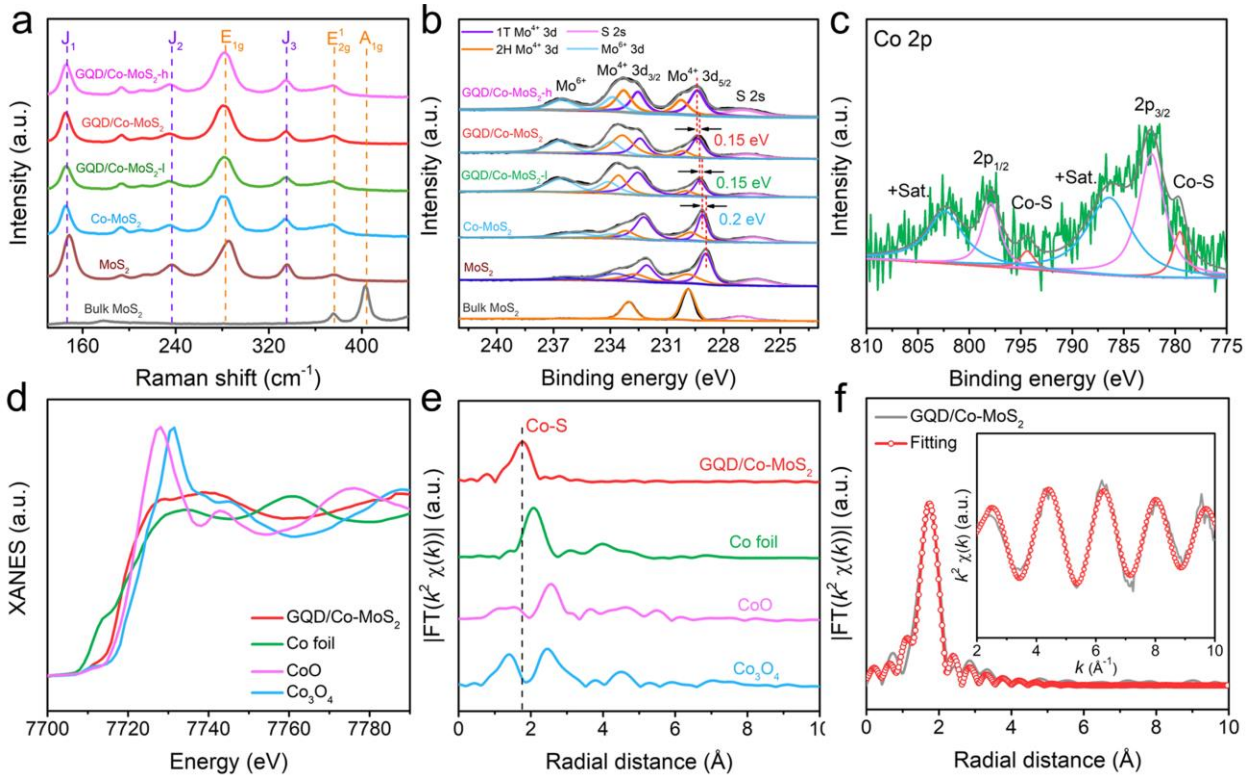

Fig. 3. Composition analysis. (a) Raman spectra and (b) XPS spectra of Mo 3d for commercial bulk MoS_2, synthesized MoS_2, Co-MoS_2, GQD/Co-MoS_2-l, GQD/Co-MoS_2 and GQD/Co-MoS_2-h; (c) Deconvoluted XPS spectra of Co 2p for GQD/Co-MoS_2; (d) Normalized XANES spectra and (e) k^2-weighted Fourier transform of EXAFS spectra at Co K-edge of GQD/Co-MoS_2 and reference samples; (f) EXAFS fitting curve of GQD/Co-MoS_2 at R-space; Inset shows the k-space EXAFS fitting curve.

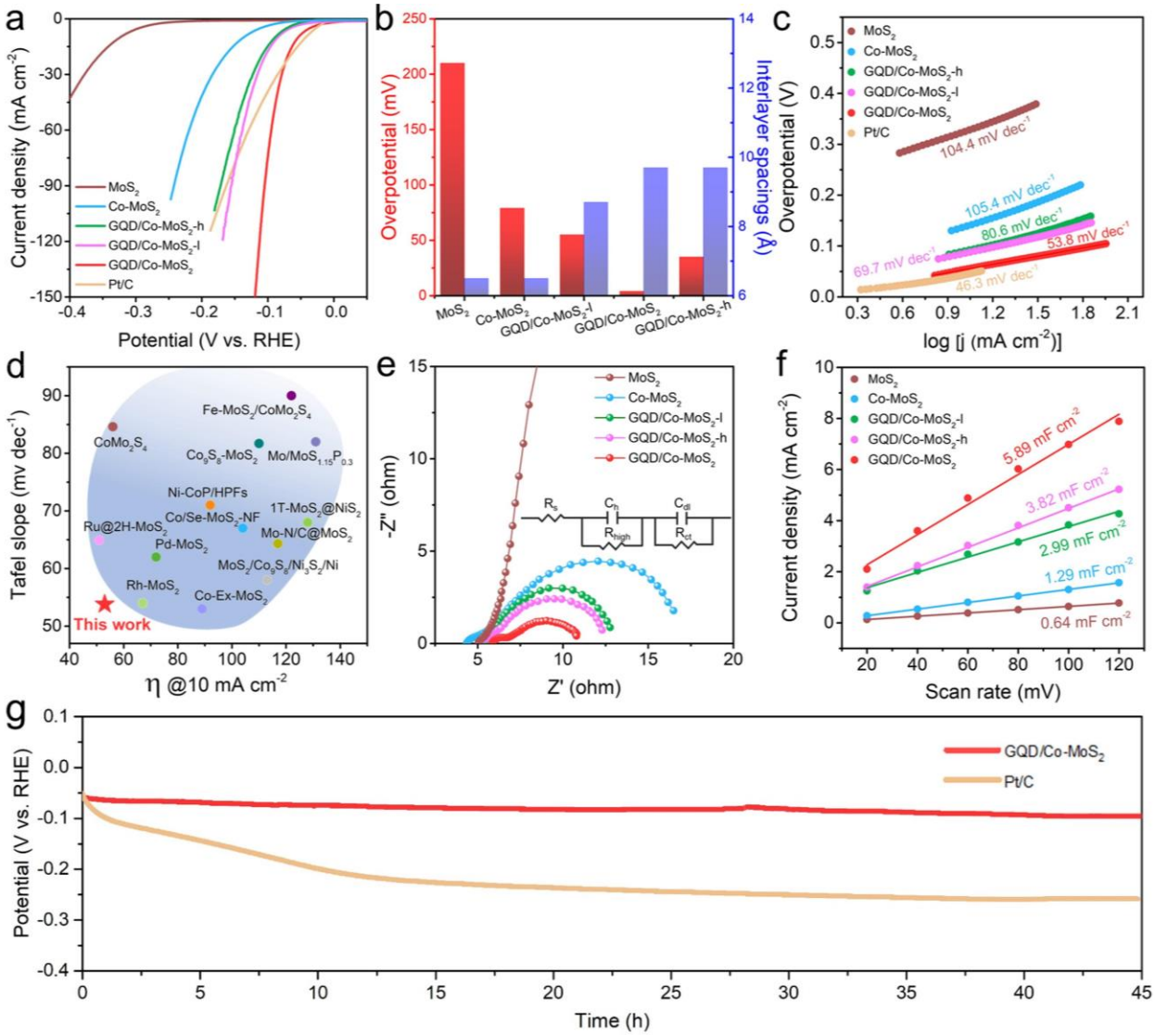

Fig. 4. Catalytic performance for HER of MoS_2, Co-MoS_2, GQD/Co-MoS_2-l, GQD/Co-MoS_2, GQD/Co-MoS_2-h, and commercial Pt/C catalyst. (a) Polarization curves; (b) Relationship between overpotential at the current density of 10 mA cm^{-2} and interlayer spacing of MoS_2 based catalysts; (c) Tafel plots; (d) Comparison with other recently reported HER electrocatalysts using 1 M KOH as electrolyte; (e) Nyquist plots from electrochemical impedance spectroscopy; (f) Charging current density difference *vs.* scan rate; (g) Stability test.

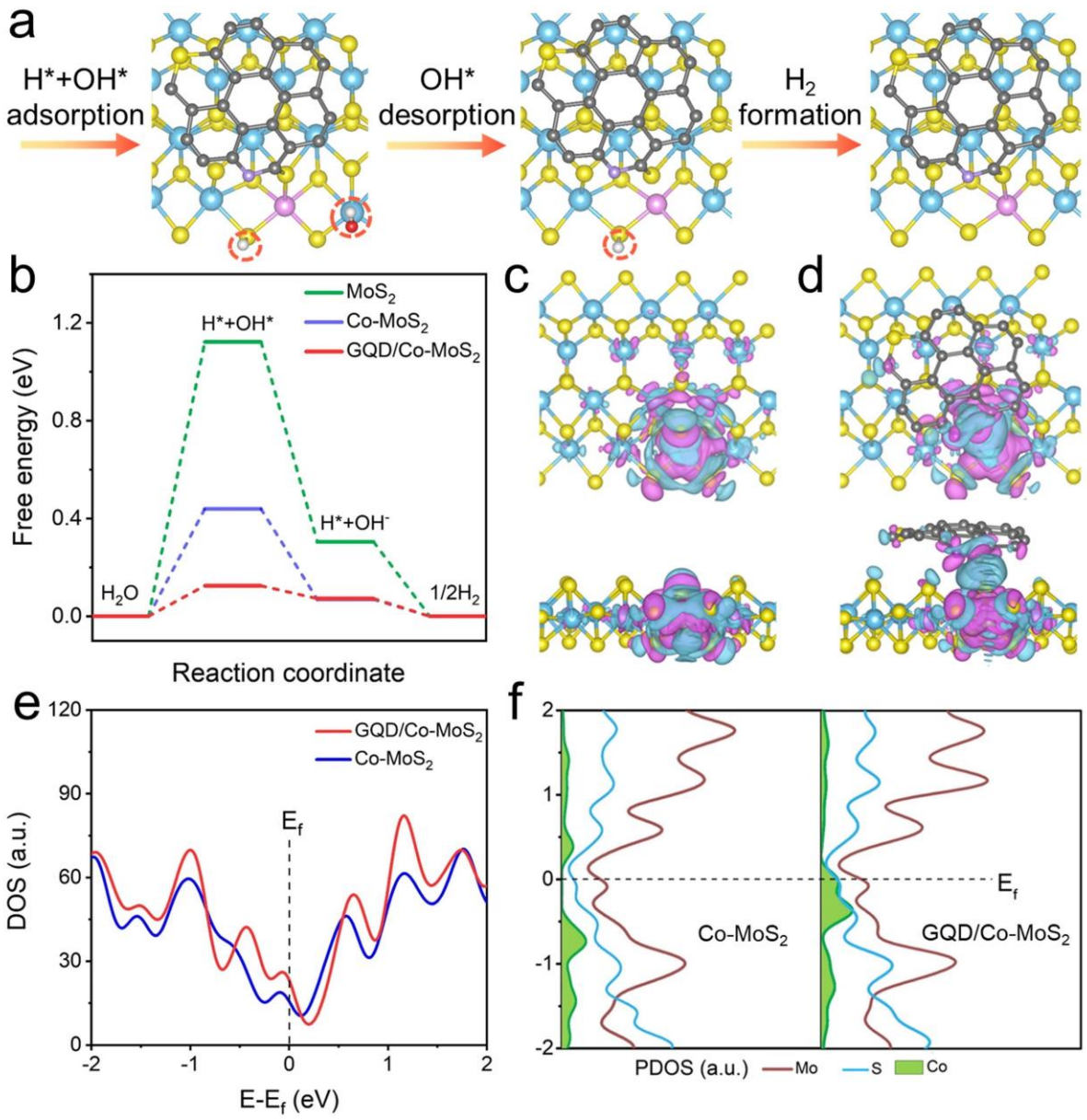

Fig. 5. DFT calculations. (a) HER reaction pathways on GQD/Co-MoS_2, in which H* and OH* are highlighted by the dash circle and the white, red, blue, yellow, dark gray, purple balls represent H, O, Mo, S, Mo, C and N atoms, respectively; (b) Free energy diagrams for HER processes catalyzed by MoS_2, Co-MoS_2, GQD/Co-MoS_2; Top and side view of electron density difference maps of (c) Co-MoS_2 and (d) GQD/Co-MoS_2, in which blue contours represent charge depletion and purple contours represent charge accumulation; (e) DOS and (f) PDOS curves.

CRediT authorship contribution statement

Jun Gong: Investigation, Methodology, Writing – original draft. **Zheye Zhang:** Investigation, Data curation, Writing – review & editing. **Shibo Xi:** Materials characterization. **Wenjun Wang:** Data curation, Writing – review & editing. **Jianmei Lu:** Writing – review & editing. **Peng Chen:** Supervision, Writing – review & editing.

Declaration of Competing Interest

The authors declare no competing financial interest.

Acknowledgments

This work was supported by an AME-IRG grant (AMEIRG18-0016) from Agency for Science, Technology and Research (A*STAR) of Singapore and the Basic Research Project of leading Technology in Jiangsu Province (BK20202012).

Appendix A. Supporting information

Supplementary data associated with this article can be found in the online version.

References

[1] M. Gong, W. Zhou, M. C. Tsai, J. Zhou, M. Guan, M. C. Lin, B. Zhang, Y. Hu, D. Y. Wang, J. Yang, S. J. Pennycook, B. J. Hwang, H. Dai, Nanoscale nickel oxide/nickel heterostructures for active hydrogen evolution electrocatalysis, Nat. Commun. 5 (2014) 4695.

[2] W. Fu, Y. Wang, W. Tian, H. Zhang, J. Li, S. Wang, Y. Wang, Non-metal single-phosphorus-atom catalysis of hydrogen evolution, Angew. Chem. Int. Ed. 59 (2020) 23791–23799.

[3] Z. Li, X. Zhang, H. Cheng, J. Liu, M. Shao, M. Wei, X. Duan, Confined synthesis of 2D nanostructured materials toward electrocatalysis, Adv. Energy Mater. 10 (2020) 1900486.

[4] X. Geng, W. Sun, W. Wu, B. Chen, A. A. Hilo, M. Benamara, H. Zhu, F. Watanabe, J. Cui, T. Chen, Pure and stable metallic phase molybdenum disulfide nanosheets for hydrogen evolution reaction, Nat. Commun. 7 (2016) 10672.

[5] S. Deng, M. Luo, C. Ai, Y. Zhang, B. Liu, L. Huang, Z. Jiang, Q. Zhang, L. Gu, S. Lin, X. Wang, L. Yu, J. Wen, J. Wang, G. Pan, X. Xia, J. Tu, Synergistic doping and intercalation: realizing deep phase modulation on MoS_2 arrays for high-efficiency hydrogen evolution reaction, Angew. Chem. Int. Ed. 58 (2019) 16289–16296.

[6] A. Bar-Hen, R. Bar-Ziv, T. Ohaion-Raz, A. Mizrahi, S. Hettler, R. Arenal, M. B. Sadan, Shelling with MoS_2: Functional CuS@MoS_2 hybrids as electrocatalysts for the oxygen reduction and hydrogen evolution reactions, Chem. Eng. J. 420 (2021) 129771.

[7] H. Cheng, Y. Diao, Q. Liu, L. Wei, X. Li, J. Chen, F. Wang, Di-nuclear metal synergistic catalysis: $Ni_2Mo_6S_6O_2$/MoS_2 two-dimensional nanosheets for hydrogen evolution reaction, Chem. Eng. J. 428 (2022), 131084.

[8] J. Feng, H. Zhou, D. Chen, T. Bian, A. Yuan, Core-shell structured ZnCo/NC@MoS_2 electrocatalysts for tunable hydrogen evolution reaction, Electrochim. Acta 331 (2020) 135445.

[9] J. Feng, H. Zhou, J. Wang, T. Bian, J. Shao, A. Yuan, MoS_2 supported on MOF-derived carbon with coreshell structure as efficient electrocatalysts for hydrogen evolution reaction, Int. J. Hydrogen Energy 45 (2018) 20538-20545.

[10] X. Wang, C. Xu, M. Jaroniec, Y. Zheng, S. Z. Qiao, Anomalous hydrogen evolution behavior in high-pH environment induced by locally generated hydronium ions, Nat. Commun. 10 (2019) 4876.

[11] C. Hu, L. Zhang, J. Gong, Recent progress made in the mechanism comprehension and design of electrocatalysts for alkaline water splitting, Energy Environ. Sci. 12 (2019) 2620-2645.

[12] K. D. Rasamani, F. Alimohammadi, Y. Sun, Interlayer-expanded MoS_2, Mater. Today. 20 (2017) 83–91.

[13] M. R. Gao, M. K. Chan, Y. Sun, Edge-terminated molybdenum disulfide with a 9.4-Å interlayer spacing for electrochemical hydrogen production, Nat. Commun. 6 (2015) 7493.

[14] J. Zhou, G. Fang, A. Pan, S. Liang, Oxygen-incorporated MoS_2 nanosheets with expanded interlayers for hydrogen evolution reaction and pseudocapacitor applications, ACS Appl. Mater. Interfaces 8 (2016) 33681–33689.

[15] H. Liang, Z. Cao, F. Ming, W. Zhang, D. H. Anjum, Y. Cui, L. Cavallo, H. N. Alshareef, Aqueous Zinc-ion storage in MoS_2 by tuning the intercalation energy, Nano Lett. 19 (2019) 3199–3206.

[16] Q. Jin, N. Liu, C. Dai, R. Xu, B. Wu, G. Yu, B. Chen, Y. Du, H_2-directing strategy on in situ synthesis of Co-MoS_2 with highly expanded interlayer for elegant HER activity and its mechanism, Adv. Energy Mater. 10 (2020) 2000291.

[17] Y. J. Tang, Y. Wang, X. L.Wang, S. L. Li, W. Huang, L. Z. Dong, C. H. Liu, Y. F. Li, Y. Q. Lan, Molybdenum disulfide/nitrogen-doped reduced graphene oxide nanocomposite with enlarged interlayer spacing for electrocatalytic hydrogen evolution, Adv. Energy Mater. 6 (2016) 1600116.

[18] N. Zahir, P. Magri, W. Luo, J. J. Gaumet, P. Pierrat, Recent advances on graphene quantum dots for electrochemical energy storage devices, Energy Environ. Mater. 5 (2022) 201–214.

[19] Y. Yan, J. Gong, J. Chen, Z. Zeng, W. Huang, K. Pu, J. Liu, P. Chen, Recent advances on graphene quantum dots: from chemistry and physics to applications, Adv. Mater. 31 (2019) 1808283.

[20] Y. Yan, D. Zhai, Y. Liu, J. Gong, J. Chen, P. Zan, Z. Zeng, S. Li, W. Huang, P. Chen, Van der Waals heterojunction between a bottom-up grown doped graphene quantum dot and graphene for photoelectrochemical water splitting, ACS Nano 14 (2020) 1185–1195.

[21] J. Gong, Z. Zhang, Z. Zeng, W. Wang, L. Kong, J. Liu, P. Chen, Graphene quantum dots assisted exfoliation of atomically-thin 2D materials and as-formed 0D/2D van der Waals heterojunction for HER, Carbon 184 (2021) 554–561.

[22] Y. Chen, Y. Cai, R. Yu, X. Pan, J. Zhang, Z. Wang, X. Xiao, J. Wu, L. Xu, L. Mai, Submerged-plant-inspired five-level-synergetic hierarchical single-Fe-atom-doped micro-electrodes for high-performance multifunctional electrocatalysis, Chem. Eng. J. 446 (2022) 136804.

[23] Z. Zhang, X. Zhao, S. Xi, L. Zhang, Z. Chen, Z. Zeng, M. Huang, H. Yang, B. Liu, S. J. Pennycook, P. Chen, Atomically dispersed cobalt trifunctional electrocatalysts with tailored coordination environment for flexible rechargeable Zn-air battery and self-driven water splitting, Adv. Energy Mater. 10 (2020) 2002896.

[24] Z. Zeng, L. Gan, H. Yang, X. Su, J. Gao, W. Liu, H. Matsumoto, J. Gong, J. Zhang, W. Cai, Z. Zhang, Y. Yan, B. Liu, P. Chen, Orbital coupling of hetero-diatomic nickel-iron site for bifunctional electrocatalysis of CO_2 reduction and oxygen evolution, Nat. Commun. 12 (2021) 4088.

[25] K. Qi, X. Cui, L. Gu, S. Yu, X. Fan, M. Luo, S. Xu, N. Li, L. Zheng, Q. Zhang, J. Ma, Y. Gong, F. Lv, K. Wang, H. Huang, W. Zhang, S. Guo, W. Zheng, P. Liu, Single-atom cobalt array bound to distorted 1T MoS_2 with ensemble effect for hydrogen evolution catalysis, Nat. Commun. 10 (2019) 5231.

[26] H. Duan, C. Wang, G. Li, H. Tan, W. Hu, L. Cai, W. Liu, N. Li, Q. Ji, Y. Wang, Y. Lu, W. Yan, F. Hu, W. Zhang, Z. Sun, Z. Qi, L. Song, S. Wei, Single-atom-layer catalysis in a MoS_2 monolayer activated by long-range ferromagnetism for the hydrogen evolution reaction: beyond single-atom catalysis, Angew. Chem. Int. Ed. 60 (2021) 7251–7258.

[27] D. Qu, M. Zheng, P. Du, Y. Zhou, L. Zhang, D. Li, H. Tan, Z. Zhao, Z. Xie, Z. Sun, Highly luminescent S, N co-doped graphene quantum dots with broad visible absorption bands for visible light photocatalysts, Nanoscale 5 (2013) 12272–12277.

[28] D. Qu, Z. Sun, M. Zheng, J. Li, Y. Zhang, G. Zhang, H. Zhao, X. Liu, Z. Xie, Three colors emission from S,N Co-doped graphene quantum dots for visible light H_2 production and bioimaging, Adv. Opt. Mater. 3 (2015) 360–367.

[29] J. Ge, D. Zhang, Y. Qin, T. Dou, M. Jiang, F. Zhang, X. Lei, Dual-metallic single Ru and Ni atoms decoration of MoS2 for high-efficiency hydrogen production, Appl. Catal. B Environ. 298 (2021) 120557.

[30] J. Li, Y. Zhang, C. Liu, L. Zheng, E. Petit, K. Qi, Y. Zhang, H. Wu, W. Wang, A. Tiberj, 3.4% solar-to-ammonia efficiency from nitrate using Fe single atomic catalyst supported on MoS_2 nanosheets, Adv. Funct. Mater. 32 (2022) 2108316.

[31] Y. Liu, Y. Huang, X. Duan, Van der Waals integration before and beyond two-dimensional materials, Nature 567 (2019) 323–333.

[32] Z. Chen, C. Liu, J. Liu, J. Li, S. Xi, X. Chi, H. Xu, I. H. Park, X. Peng, X. Li, Cobalt single-atom-intercalated molybdenum disulfide for sulfide oxidation with exceptional chemoselectivity, Adv. Mater. 32 (2020) 1906437.

[33] Z. Luo, Y. Ouyang, H. Zhang, M. Xiao, J. Ge, Z. Jiang, J. Wang, D. Tang, X. Cao, C. Liu, Chemically activating MoS_2 via spontaneous atomic palladium interfacial doping towards efficient hydrogen evolution, Nat. Commun. 9 (2018) 2120.

[34] Z. Liu, L. Zhao, Y. Liu, Z. Gao, S. Yuan, X. Li, N. Li, S. Miao, Vertical nanosheet array of 1T phase MoS_2 for efficient and stable hydrogen evolution, Appl. Catal. B Environ. 246 (2019) 296-302.

[35] Y. Li, K. Chang, Z. Sun, E. Shangguan, H. Tang, B. Li, J. Sun, Z. Chang, Selective preparation of 1T- and 2H-Phase MoS_2 nanosheets with abundant monolayer structure and their applications in energy storage devices, ACS Appl. Energy Mater. 3 (2019) 998–1009.

[36] S. Wang, D. Zhang, B. Li, C. Zhang, Z. Du, H. Yin, X. Bi, S. Yang, Ultrastable in-plane 1T-2H MoS_2 heterostructures for enhanced hydrogen evolution reaction, Adv. Energy Mater. 8 (2018) 1801345.

[37] J. Luxa, P. Vosecký, V. Mazánek, D. Sedmidubský, M. Pumera, Z. k. Sofer, Cation-controlled electrocatalytical activity of transition-metal disulfides, ACS Catal. 8 (2018) 2774–2781.

[38] M. Wu, J. Zhan, K. Wu, Z. Li, L. Wang, B. Geng, L. Wang, D. Pan, Metallic 1T MoS_2 nanosheet arrays vertically grown on activated carbon fiber cloth for enhanced Li-ion storage performance, J. Mater. Chem. A 5 (2017) 14061–14069.

[39] X. Shan, J. Liu, H. Mu, Y. Xiao, B. Mei, W. Liu, G. Lin, Z. Jiang, L. Wen, L. Jiang, An engineered superhydrophilic/superaerophobic electrocatalyst composed of the supported CoMoSx chalcogel for overall water splitting, Angew. Chem. Int. Ed. 59 (2020) 1659–1665.

[40] Q. Xiong, Y. Wang, P. F. Liu, L. R. Zheng, G. Wang, H. G. Yang, P. K. Wong, H. Zhang, H. Zhao, Cobalt covalent doping in MoS_2 to induce bifunctionality of overall water splitting, Adv. Mater. 30 (2018) 1801450.

[41] C. Lei, Y. Wang, Y. Hou, P. Liu, J. Yang, T. Zhang, X. Zhuang, M. Chen, B. Yang, L. Lei, Recent progress made in the mechanism comprehension and design of electrocatalysts for alkaline water splitting, Energy Environ. Sci. 12 (2019) 149–156.

[42] X. Dai, K. Du, Z. Li, M. Liu, Y. Ma, H. Sun, X. Zhang, Y. Yang, Co-doped MoS_2 nanosheets with the dominant CoMoS phase coated on carbon as an excellent electrocatalyst for hydrogen evolution, ACS Appl. Mater. Interfaces 7 (2015) 27242−27253.